To cite this version :

Malo LECORGNE, Emmanuelle ABISSET-CHAVANNE, Marie-Marthe GROZ, Alain SOMMIER, Christophe PRADERE - A study on real-time quantitative thermal analysis of composite tapes - NDT& E International - Vol. 144, p.103096 - 2024

A study on real-time quantitative thermal analysis of composite tapes

M. Lecorgne [a],[*], E. Abisset-Chavanne [a], M-M. Groz [a], A. Sommier [a], C. Pradère [b]

[a] I2M TREFLE, UMR 5295 CNRS-UB-ENSAM, 351 Cours de la Libération, 33400 Talence, France
[b] EPSYL-Alcen, Esplanade des Arts et Métiers, CEDEX, 33405 Talence, France

ABSTRACT

Keywords:
Non destructive control
Thermal method
Composite
Real time

Generating vast volumes of data by continuously moving systems in industrial environments presents a significant challenge. The carbon fiber reinforced polymer (CFRP) tapes control exemplifies this issue, with a strongly increasing production these last decades, and yielding several tens of meters to inspect within a short time. It leads to a pressing need for rapid and effective quality control and decision-making systems. This study introduces an innovative method for mitigating data overload by focusing on the defective sections of the tape by creating a corresponding virtual twin to assess fiber content variations. Data analysis techniques are employed to differentiate flawless from faulty regions and thermal methods are applied to characterize observed defects. This article presents a comprehensive approach for enabling the analysis of tens of meters of tapes at 25 cm/s speed scroll within a competitive timeframe.

Introduction

Recently, Carbone Fiber Reinforced Polymer (CFRP) production has been strongly increasing, reaching 181 kilotonnes (kt) in 2021, and predicted to reach 285kt in 2025 [1]. Hence, the production of CFRP tape, which is the focus of this study, has also undergone a substantial increase [2]. This rise can be attributed to the material's desirable characteristics, including its lightweight nature, excellent mechanical properties, and cost-effective production. The control of these CFRP tapes is a significant and extensively studied challenge in modern engineering. These tapes exhibit high anisotropy and complexity, finding widespread application in the aerospace, oil & gas, and automotive sectors. Moreover, during the last decade, CFRP automated fiber placement has steadily increased, rising from 7% in the 1990s to 35% in 2020 [3]. Ensuring effective control of CFRP tape is essential for achieving the high operability of the automated system and optimizing the performance of the final composite.

One of the key parameters to control in order to obtain favorable interfacial properties in multilayer manufacturing is the proper fiber placement [4]. Defects arising from uneven weaving or variations in the fiber content of the tape can significantly impact the final laminate mechanical properties [5]. For instance, a low fiber content affects mechanical characteristics, while an excessive content results in reduced matrix requirements for tape bonding. Due to high demand in various applications, CFRP tapes are typically produced in rolls spanning several hundreds of meters.

In the context of long industrial pieces, the most common and expedient control approach involves a system capable of acquiring and processing data in real time. Such a control system relies on non-destructive and contactless physical methods, with various options available based on different physical principles, such as optics [6], radio frequencies [7], eddy currents inspection [8] and induction [9]. Among these methods, Line Scan Thermography (LST) [10] stands out due to its ability to detect and characterize defects and its ease of implementation on a control line [11]. This study focuses on this particular method for CFRP tape inspection for the detection and characterization of fiber content variations as defects.

Prior investigations have delved into the realm of defect detection using infrared thermography. An initial study [11] demonstrated its efficacy in this context, particularly in detecting various flaws, including issues related to fiber/matrix distribution. This work substantiated the potential of thermography for defect detection. To harness its capabilities, it is often coupled with the Pseudo-Static Matrix Reconstruction (PSMR) algorithm [12,13]. This integration facilitates the utilization of conventional techniques employed in Pulsed Thermography (PT), such as Pulsed Phase Thermography (PPT), Pulsed Least Squares Thermography (PLST), and Principal Components Thermography (PCT) [14]. A comparative analysis between PT and LST systems reveals that LST not only provides a superior Signal-to-Noise Ratio (SNR) but also enhances image contrast [15]. In an attempt to bypass the PSMR algorithm and work with Dynamic Thermograms, an alternative approach was developed [16]. A Discrete Fourier Transform is applied on each pixel to reveal variations due to a defect. Because these phase variations can appear at different Fourier frequencies, defect
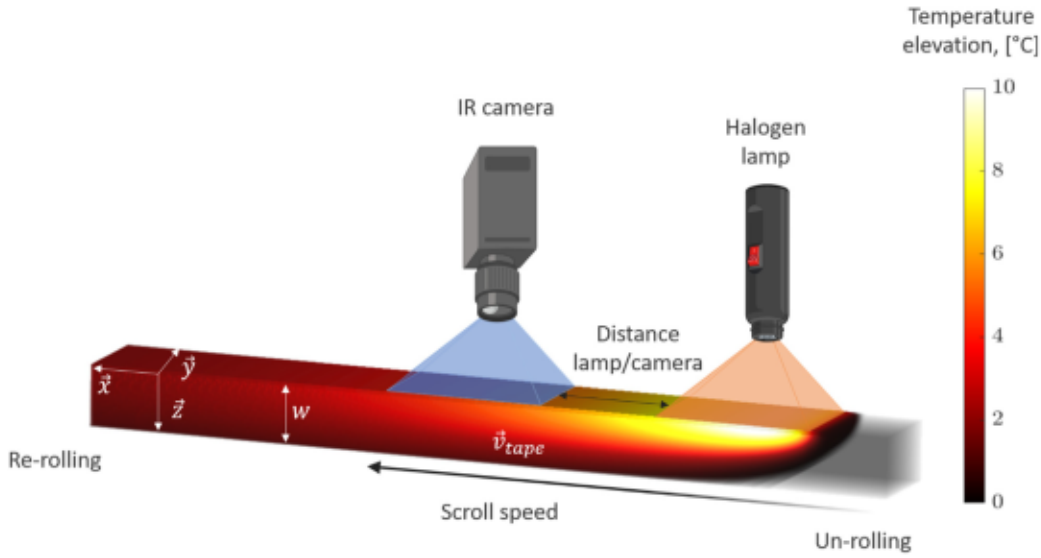

Fig. 1. Setup of the LST. The width w is resized with a factor of 5 to improve the readability of the figure. The tape is in motion, unrolling from one side of the control system and rolling up on the other side.

detection can be robustified by reducing the noise effect. However, this methodology suffers from the drawback of being unable to generate the cooling curve for a specific point, which is essential for accurate quantification. Furthermore, several studies emphasize the significance of meticulously selecting parameters to optimize defect detection, [17]. Nevertheless, the context changes when dealing with extremely thin materials, measuring less than 300 μm in thickness. In such cases, a reassessment of these parameters becomes imperative. Moreover, an algorithm designed for quantifying depth (whether in the first or second half of the tape) and determining fiber content is indispensable. Such an algorithm should seamlessly integrate with the physical system and the detection methods appplied. Remarkably, for composite tapes, such a comprehensive algorithm is currently non-existent but warrants development.

Adhering to the principles of Industry 4.0 [18], this study aims to achieve real-time processing of big data. To this end, we present a comprehensive algorithm that employs data-derived thresholds for defect detection, substantially reducing the volume of data required for analysis. A stochastic method is subsequently applied to quantify observations. Ultimately, our findings enable the creation of a virtual twin, providing a representation of the tape's characteristics where defects can be detected.

1. Materials and model

1.1. Materials

The setup configuration for tape analysis is depicted in Fig. 1. The tape is initially in a rolled form and undergoes a sequence of operations at constant speed: (1) it is unrolled from one side ; (2) it is passed in front of the control system, which includes an halogen lamp, followed by an infra-red (IR) camera ; (3) finally, it is re-rolled on the other side. The IR camera utilized is a FLIR quantum camera with a frequency of 300 Hz and a spatial resolution of 160 μm. The heating system is an halogen ramp.

The material under investigation in this study is a thin tape with a thickness of 250 μm, consisting of longitudinal carbon fibers embedded in a matrix of PEEK (*Poly-Ether-Ether-Ketone*). The pertinent properties of both components are summarized in Table 1. Two distinct mixing laws are utilizing to calculate the conductivity k of the tape, by employing a combination of the conductivities from the fibers and matrix: the Voigt model for conductivity parallel to the direction of the fibers,
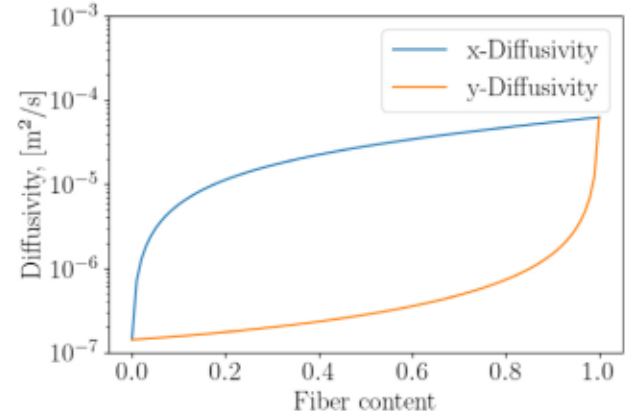

Fig. 2. Variation of the diffusivities along the x and y directions according to the fiber content.

and the Reuss model for the one perpendicular to the fibers [19]. Thus, the conductivity k can be determined using Eq. (1), representing both mixing laws with α the fiber content. The tape density ρ, and heat capacity c_p are calculated with the Voigt model. Henceforth, we also denote the thermal diffusivity by a. The variables indexing by x, y or z are variables for the given direction. The diffusivities variations are plotted in Fig. 2. In this study, the controlled composite's fiber content is set at 0.5.

$$\begin{cases} k_{\parallel} = \alpha k_{fiber} + (1-\alpha)k_{matrix} \\ k_{\perp} = \dfrac{1}{\alpha k_{fiber} + (1-\alpha)k_{matrix}} \end{cases} \quad (1)$$

From this mixing law, it is possible to calculate different Fourier numbers as defined in Eq. (2).

$$F_{o_z} = \frac{a_z L_c}{v L_z^2} \quad (2)$$

A first Fourier number can be defined to check the time under the lamp is much lower than the depth diffusion time. In this case L_c is the width of the heated area. In this case, the Fourier has to verify $F_{o_1} \ll 1$ [20]. This will improve the sensibility to a defect in depth after the lamp. A second one can be calculated, to define the size of the camera window L_x required for capturing in-depth information. Here the characteristic length is L_x and is set to verify the following condition: $F_{o_2} \approx 1$. With

Table 1
Material parameters of the model.

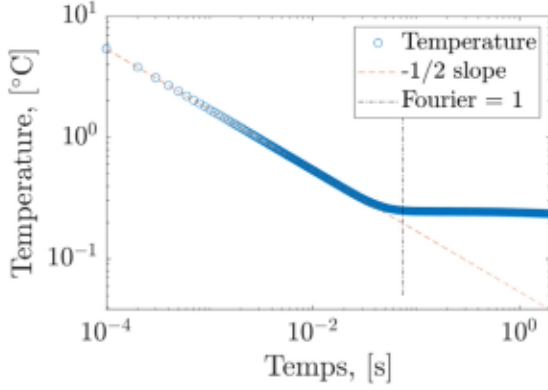|	Thermal conductivity λ (W m^{-1} K^{-1})	Density ρ (kg m^{-3})	Heat capacity c_p (J K^{-1} kg^{-1})	Thermal diffusivity a (m^2 s^{-1})
Carbon fibers	100	2 000	800	$6.25e^{-5}$
PEEK	0.25	1 320	1 340	$1.4e^{-7}$

Fig. 3. Illustration of the Fourier = 1 on the loglog cooling thermogram after a pulse. The inflection point indicates the limit of 1D heat transfer due to the sample's width.

a lower Fourier number the diffusion has not reached the back of the tape. For a higher one, the system is balancing, the maximum contrast peak is exceeded so no more in-depth information can be obtained. In the specific case of the material studied, the second Fourier number is achieved at 0.04s after a static pulse (see Fig. 3).

1.2. Direct model

To model the heat diffusion through a homogeneous section of a moving tape, the quadripoles method provides an analytical approach [21]. Considering the insights gained from the thermal study of Section 1.1 and assuming the system is symmetrical so the diffusion in the plane perpendicular direction can be neglected, the problem can be simplified to a two-dimensional system, encompassing the depth and length dimensions (see Fig. 4). In this scenario, the heat equation includes a transport term. It corresponds to the movement of the tape. Its speed v_{tape} is quoted v in the model to simplify the writing. We assume a temperature of T_∞ well before the heat flux and a null flux far beyond. Consequently, the system is described by the following set of equations (see Eqs. (3)):

$$
\begin{cases}
\dfrac{\partial^2 T}{\partial z^2} + \dfrac{a_x}{a_z}\dfrac{\partial T}{\partial x^2} - \dfrac{v}{a_z}\dfrac{\partial T}{\partial x} = 0 \\
T(x=0, z, t) = T_\infty \\
\dfrac{\partial T(x,y,t)}{\partial x}\Big|_{x \to +\infty} = 0 \\
-\lambda \dfrac{\partial T(x,y,t)}{\partial z}\Big|_{z=e} = -h(T - T_\infty) \\
-\lambda \dfrac{\partial T(x,y,t)}{\partial z}\Big|_{z=0} = \phi_e(x) - h(T - T_\infty)
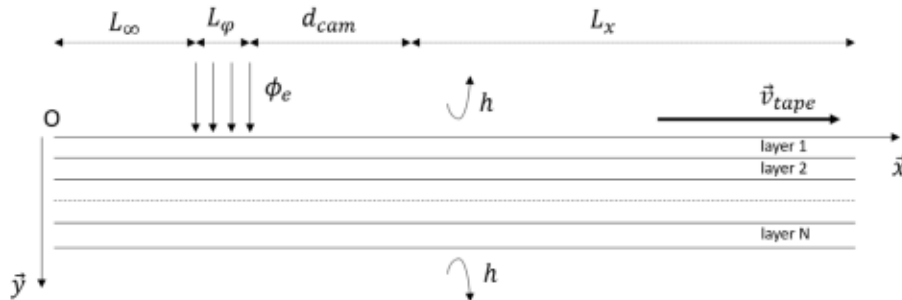\end{cases}
\tag{3}
$$

with the flux of power Q defined as a spatial step (equation (4)):

$$
\phi_e(x) =
\begin{cases}
Q & \text{if } L_\infty \leq x \leq L_\infty + L_\phi \\
0 & \text{else}
\end{cases}
\tag{4}
$$

This can be expressed in the Laplace domain, with the standard quadripoles form (equation (5)), quoting p the Laplace variable along x, $\theta = \mathcal{L}(T - T_\infty)$ and $\Phi = \mathcal{L}(\phi)$:

$$
\begin{bmatrix} \theta_e \\ \Phi_e - h\theta_e \end{bmatrix} =
\begin{bmatrix} cosh(\gamma e) & \frac{1}{\lambda \gamma S} sinh(\gamma e) \\ \lambda \gamma S \, sinh(\gamma e) & cosh(\gamma e) \end{bmatrix}
\begin{bmatrix} \theta_s \\ h\theta_s \end{bmatrix}
\tag{5}
$$

with $\gamma^2 = \frac{a_x}{a_z}p^2 - \frac{v}{a_z}p$. The heat flux Φ_e in the Laplace domain is given by:

$$
\Phi_e(p) = \frac{Q}{p}exp(-pL_\infty)(1 - exp(-pL_\phi))
\tag{6}
$$

It can be readily be extended to a N-multilayer material including thermal resistances R_i between the layers as (7):

$$
\begin{bmatrix} \theta_e \\ \Phi_e - h\theta_e \end{bmatrix} =
\prod_{i=1}^{N}
\begin{bmatrix} A_i & B_i \\ C_i & D_i \end{bmatrix}
\begin{bmatrix} 1 & R_i \\ 0 & 1 \end{bmatrix}
\begin{bmatrix} \theta_s \\ h\theta_s \end{bmatrix}
\tag{7}
$$

with A_i, B_i, C_i and D_i the components of the matrix of Eq. (5) for each layer i of thickness e_i and material parameters λ_i, ρ_i, c_{p_i} and a_i. For a single layer, the surface temperature can be calculated with the following expression:

$$
\Theta(p) = \frac{cosh(\gamma e)}{\lambda \gamma \, sinh(\gamma e)}\Phi(p)
\tag{8}
$$

In this context, the parameters to be estimated are the diffusivities along each direction, which are linked to the fiber content through Eq. (1). Several examples of thermograms with varying fiber contents are displayed in Fig. 5. In the same figure, thermograms are plotted on two distances after the lamp: $d_{cam} = 0$ cm and $d_{cam} = 2$ cm. In Section 2 the optimized distance will be specified.

For the sake of clarity, the various model parameters and their sensitivities are presented in the Table 2.

2. Study to optimize the camera field of view

One highly sensitive parameter in the model is the camera field of view, which can also be viewed as the lamp/camera distance. This section is dedicated to determining the optimal choice between the two options presented in Fig. 5 to improve sensitivity on the fiber content. No in-depth information is needed in our study. In the figure, it appears that a camera field of view between 0 cm and 1 cm is
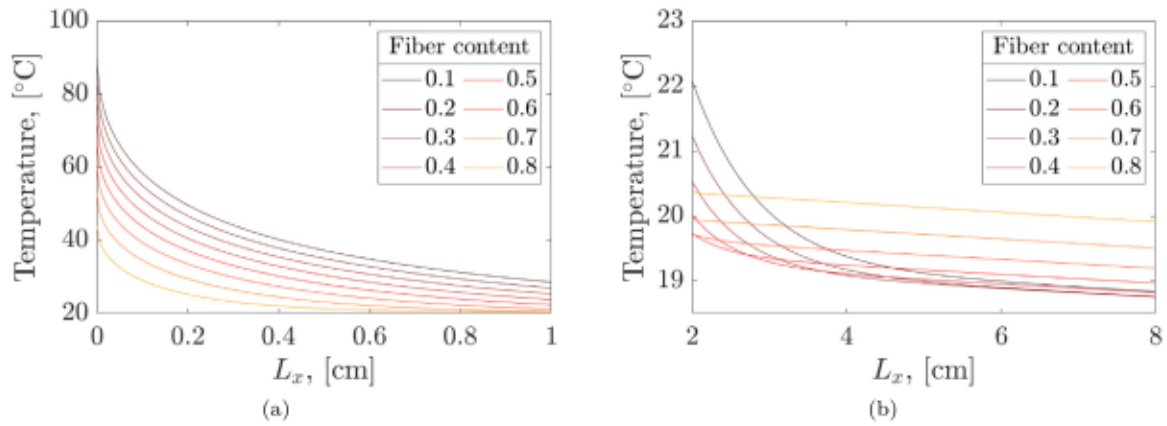

Fig. 4. Complete schema of the problem of the moving tape. The different notations are: h the convection coefficient, ϕ the heat flux of the lamp with its width L_ϕ, L_∞ the distance to infinity before the lamp, d_{cam} the distance between the lamp and the camera and L_x the camera field of view. In this control system, the lamp and camera remain stationary, while the tape moves at a speed $\vec{v}_{tape}$.

Fig. 5. (a) Examples of different fiber content thermograms obtained. (b) A zoom is performed on the optimized camera field of view between 2 cm and 8 cm after the heating lamp (see Section 2).

Table 2
Model parameters sensitivity.

	Fiber content	Velocity	Convection	Flux width	Camera field of view	Camera frequency
Sensitivity	High	Medium	Low	Low	High	–
Measurement	Unknown parameter to estimate	Measured in real-time	$h = 18\,\mathrm{W}$ $\mathrm{m}^{-2}\,\mathrm{K}^{-1}$	Fixed	Optimized	Optimized

the most suitable due to its heightened sensitivity to temperature changes according to the fiber content. However, when employing the characterization method (presented in Section 3.4), due to the absence of a reference thermogram for the background (*i.e.* when the tape is motionless and the lamp is turned off) during system operation and to facilitate comparison with the model, a normalization becomes imperative. The normalization method involves subtracting the last recorded temperature value from all the thermograms followed by division by the thermogram's maximum value. Then, the optimization is performed on the normalized thermograms presented in Figs. 6(a) and 6(b). The normalized temperature is denoted as T^*.

Based on the reduced sensitivity results after normalization (Figs. 6(c) and 6(d)), it finally seems more appropriate to set the camera field of view between 2 cm and 8 cm. This choice is informed by the fact that the highest sensitivity to fiber content is located around the median fiber content (0.5), and it is much lower at the extremes. Consequently, the estimation of fiber content will be most accurate around the mean value. Also, although the fiber content is not well estimated at the extremes, this approach enhances the differentiation between excessively high and excessively low fiber content. Hence, even though the temperature sensitivity is relatively low, it remains satisfactory in terms of Signal-to-Noise Ratio (SNR) when using a camera with 0.1K performance.

3. Image processing method

The overall method proposed in this study consists of several distinct blocks: threshold definition, velocity measurement, defect detection, static thermogram reconstruction, quantification of defects, and the creation of the final virtual twin representing the properties. The algorithm's schematic representation is illustrated in Fig. 7.

In all of the following sections, T is the temperature from the model while DL are Digital Level returned by the IR camera and linked to the experimental temperature.

3.1. Threshold definition

Initially, given the substantial volume of data acquired by the control system, a rapid segmentation process is imperative to isolate the frames containing defects. This constitutes the initial preprocessing step depicted in the flowchart in Fig. 7. An adaptative threshold s is determined in real time by taking into account both the intensity and the size of the defects. Indeed, the size of the defect regions must encompass multiple pixels to mitigate false positives resulting from noise. The thresholds are set spatially and temporally, specifically for each spatial increment in the rolling direction and within a shifting time interval. This loop evolves during the scan to improve adaptability and adjusts to exterior disturbances.

To achieve this, a statistical study is carried out on the intensities' distribution to define two distinct defect detection criteria, for "hot" and "cold" area (below or above the mean), assuming the proportion and deviation of this two populations from the mean are different. When observing the Henry curve in the case of a skewed normal distribution, we notice a well correspondence for the average population, but not for the high extreme values (Fig. 8). This discrepancy can be attributed to the presence of a significant number of minor hot spots. Indeed, in the event of a defect occurring within the camera's field of view, whether the fiber content is low or high, the intensity surpasses the mean, as observed in Fig. 5(b). Therefore, this lack of distribution conformity observation is further emphasized by the presence of defects in the analyzed images.

Considering that the distribution deviates significantly from a normal distribution, particularly in the case of hot spots, various threshold methods are compared. We chose to investigate three methods that appear suitable and have been used in the literature, for example in the work of L. Smalaky et al. [22].

3.1.1. Threshold from average deviation method

Firstly, despite the non-Gaussian nature of the distribution on the maxima, the Gaussian assumption is consistent for the remainder of the histogram. A threshold can be simply defined as the deviation from the mean over time and the tape width (y direction) :

$$s(x) = \mu(x) - n \cdot \sigma(x) \qquad (9)$$

with μ the mean, σ the standard deviation and n the parameter setting the distance from the mean. The variables x and y represent spatial coordinates. Its computational time is about 3 s for 5,000 frames used.
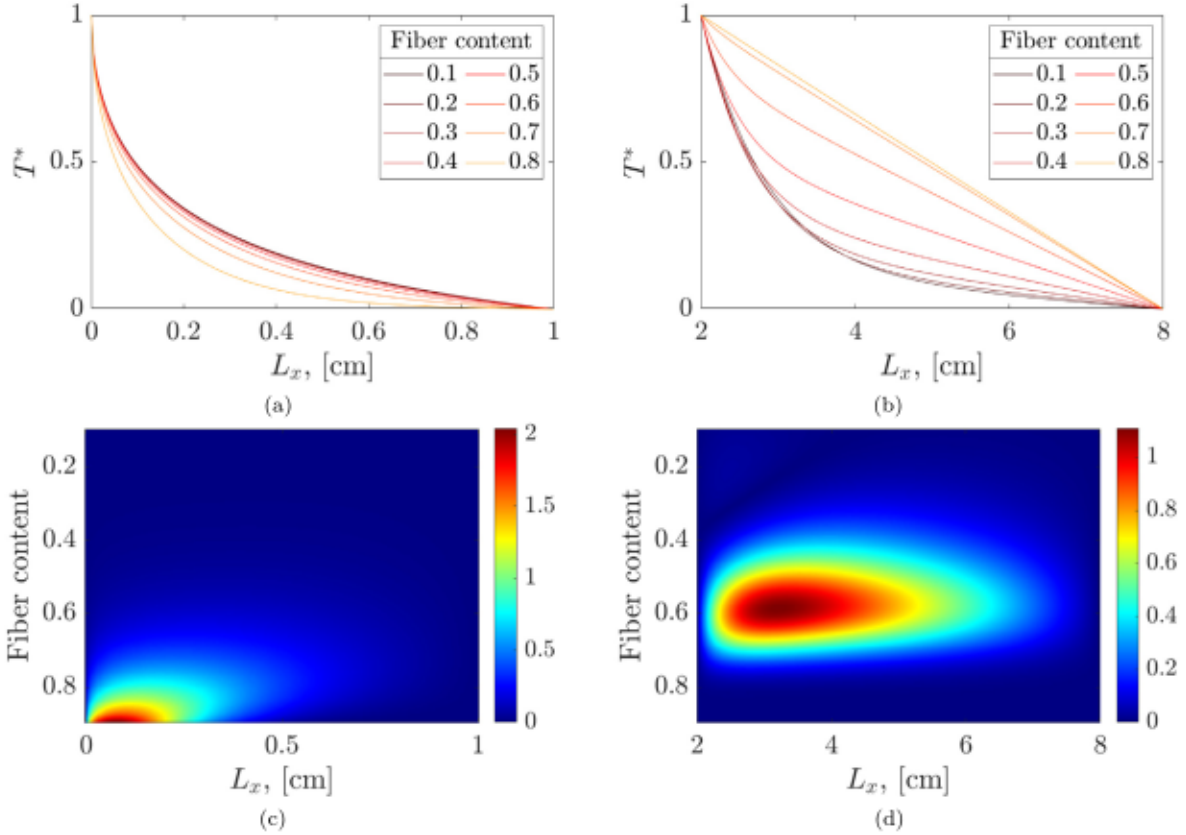
Fig. 6. Top (a and b): Examples of normalized thermograms obtained from different fiber content. The normalization method involves subtracting the last recorded temperature value from all the thermograms followed by division by the thermogram's maximum value. Bottom (c and d): Corresponding reduced sensitivity according to the fiber content. The colorbar units represent temperature (°C), obtained with reducing sensitivity analysis based on the fiber content parameter.

3.1.2. Threshold derived from temperature extrema

The concept of this criteria involves treating defects as either hot or cold spots, corresponding to the extrema of the distribution. By plotting the maxima or minima over time and the tape width (y direction), the distribution of average defect intensity is obtained. A second threshold can thus be established to segregate anomalies among the extrema distribution, using the same method as described in Section 3.1.1. Fig. 9 illustrates the method. This threshold is higher than the previous one in the nearby area of the lamp as it utilizes only the extrema of the intensity distribution. Its computational time is about 1 s for 5,000 frames used.

3.1.3. Threshold from the Yen method

This method is well-suited for subtracting objects from the background, making it applicable here to segregate defects from the average intensity based on the temperature maxima, without the need for any parameter adjustments. It allows the computation of the upper threshold based on the intensity distribution of pixels belonging to a column over time. The algorithm employed to define the threshold is the Yen algorithm [23]. It is a slower algorithm compared to others ($\approx$ 7 s to compute for 5,000 frames used), and it operates automatically without parameters to change, which is advantageous for automation but may be less controllable.

3.1.4. Comparison

All the different methods yield effective results in defect detection, each exhibiting distinct tolerances and computational times. For this study, we opted to utilize the extrema method based on extrema, as it produces fewer artifacts compared to the "$\mu - n\sigma$" method and is less noisy than the threshold derived from Yen's method, while also being faster (see Fig. 10). The method is configured with a parameter n set to 2.

3.2. Velocity measurement

Simultaneously with the preceding section, as illustrated in Fig. 7, velocity measurement was conducted. This parameter holds significant importance in defect tracking, for the model's performance and characterization. To ensure an efficient velocity measurement, we adopt a method that entails tracking hot or cold spots, as detailed in [24]. By plotting a row of the film in the x-direction over time, when hot spots appear, their motion creates distinct lines with slopes that are proportional to the velocity (Fig. 11(a), left side). To extract these slopes, an edge detection algorithm is utilized. One of the most popular, the Canny filter [25], is applied to the image. All the lines are thus detected as edges (Fig. 11(a), right side). The output of the filter generates a matrix with ones on the detected edges and zeros elsewhere. Subsequently, a labeling process is applied to this output. Following segmentation of the largest continuously labeled lines, when the linear regression coefficient is close to 1, indicating reliable velocity estimation, the slope and the velocity are calculated. The final velocity is the average of the various calculated velocities across all the rows of the film. This method enables the calculation of longitudinal velocity without any external sensors, offering high precision (average error above 1.5% compared to the ordered value) and stability over time, as shown in Fig. 11(b).

3.3. Defect tracking and static thermograms reconstruction

Both defect detection and tracking work jointly. This is the idea of tracking by detection used in computer vision [26]. Utilizing the
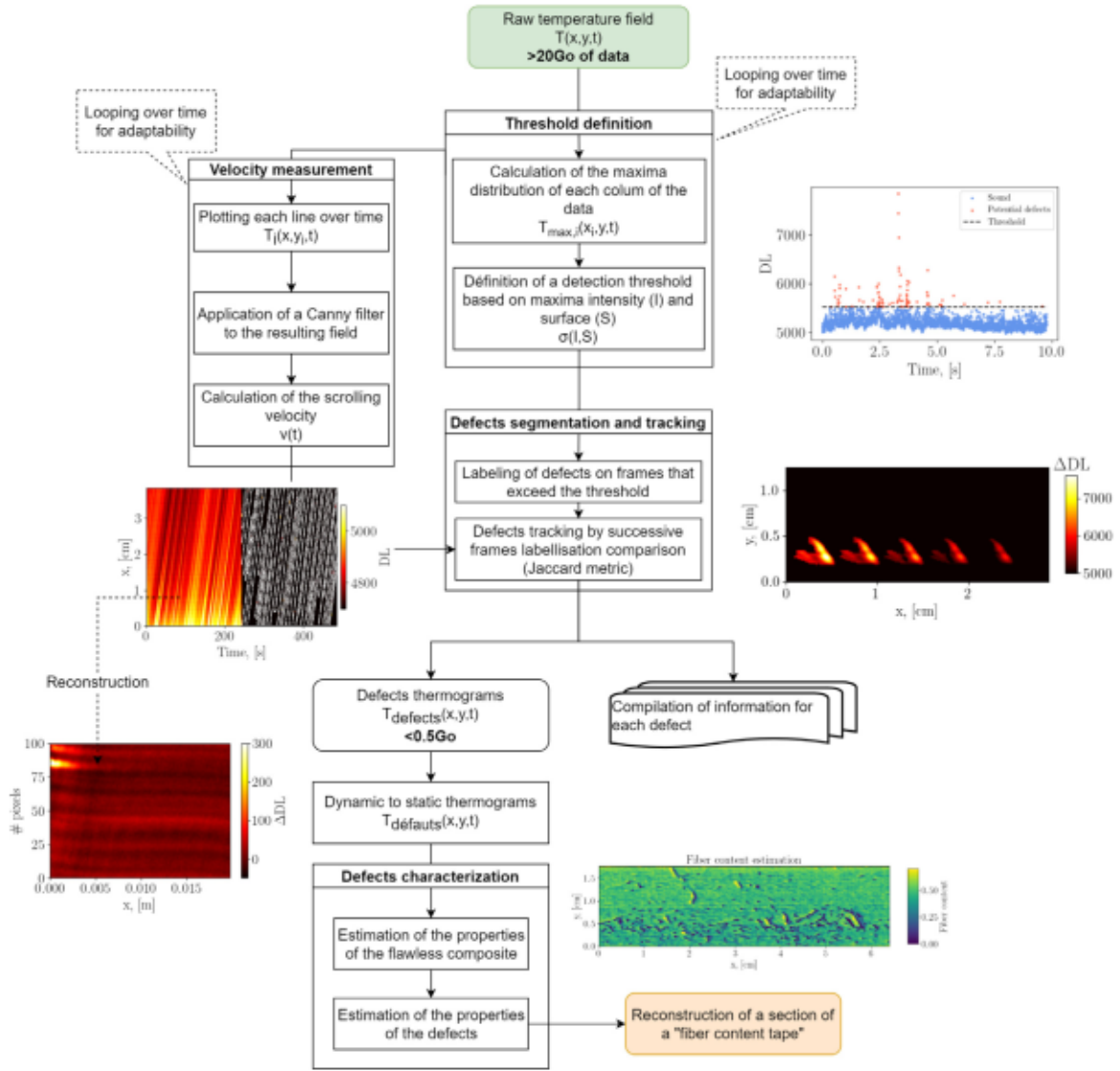
Fig. 7. Flowchart summarizing the algorithm, from raw thermal images into a virtual twin of the tape fiber content.

established threshold outlined in Section 3.1, defects are labeled within the frames where they occur. Then, to identify corresponding defects, a comparison is made between two consecutive labeled images, with the first one being shifted to the right according to the velocity data acquired in Section 3.2. The confidence of correspondance is measured with the Jaccard metric [27] as illustrated in Fig. 12. Each defect is assigned a unique number, enabling individual defect tracking, and recording various properties (including location, time of appearance, frequency of occurrence and maximum and minimum intensity).

The inversion process was deployed by constructing pseudo-static thermograms given the scrolling speed v and using the PSMR method. Each were based on the dynamic thermograms captured directly by the camera (Eq. (10)).

$$T(t_0 + \Delta t, x_0 + \frac{v}{\Delta t}) \Rightarrow T(t_0 + \Delta t) \qquad (10)$$

This implies that for each time step, the constructed temperature field is shifted by the discretized velocity $\frac{vf}{s_p}$, where v represents the velocity, f is the frequency, and s_p corresponds to the size of a pixel (as illustrated in Fig. 11(a)). Interpolation is applied when the discretized velocity is non-integer. It is worth noting that errors in the reconstruction can arise when using wide-angle cameras, potentially introducing distortions at the image edges. Therefore, a preliminary correction step is necessary to improve the reconstruction accuracy.

3.4. Defect characterization

The final stage of the developed global algorithm, as depicted in Fig. 7, focuses on defect characterization. Once a defect is detected and the pseudo-matrix is reconstructed, the objective is to estimate its diffusivity, which is closely linked to the fiber content. To accomplish this task in real time, a stochastic algorithm is employed. This choice is motivated by its efficiency in terms of computational speed, as it ensures low computer processing time. Furthermore, not only does this stochastic approach provides the optimal estimate of the fiber content but it also offers insights into the probability distribution associated with this parameter across the entire defined domain.

The estimation method employed in this study is based on Bayesian inference, derived from Bayes' formula [28] (equation (11)), where β represents the fiber content, and T_{obs} denotes the temperature field.

$$\pi(\beta|T_{obs}) = \frac{\pi(T_{obs}|\beta)\pi(\beta)}{\pi(T_{obs})} \qquad (11)$$

In the formula, the left term is the *a posteriori* probability density, utilized to assess the parameters that best fit the observed data. On the right-hand side, the term $\pi(T_{obs})$ corresponds to the marginal probability of the measurement, treated as a constant to normalize the *a posteriori* probability. The term $\pi(\beta)$ represents the probability density
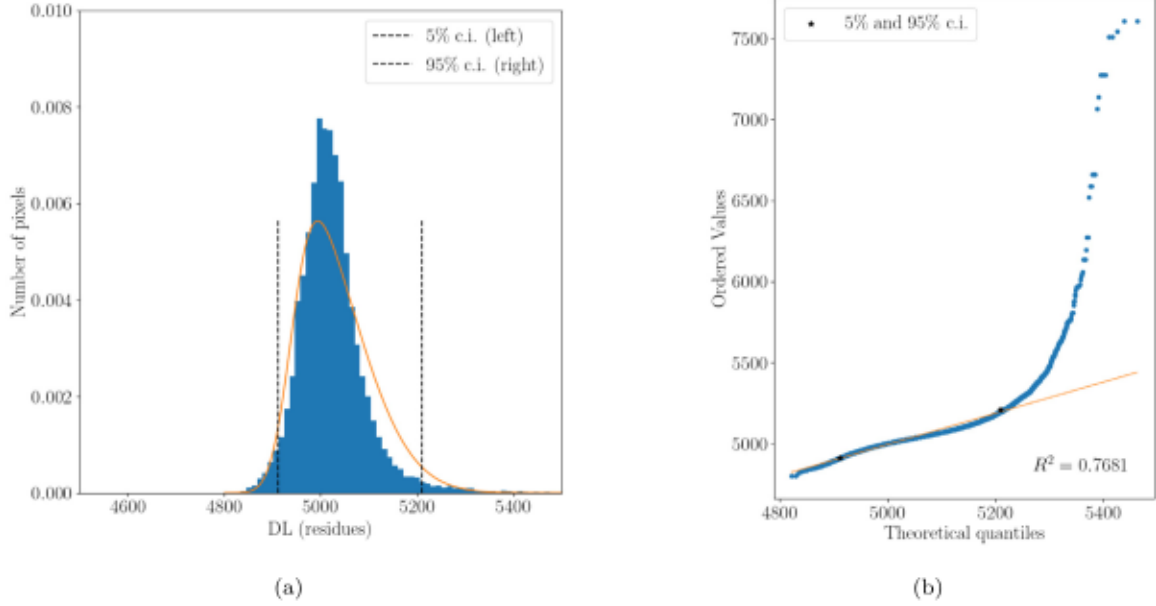
Fig. 8. (a) Density distribution of the residuals intensities of 50,000 random pixels of one column across 1,000 frames. Comparison with a skew normal distribution (in orange). The parameters of the closest skewnorm distribution are evaluated with the function *fit* of the Python library *scipy.stats.skewnorm*. (b) Henry curve represnetation of the distribution. The black markers indicate the 5% and 95% quantiles. We observe a distribution that is reliably similar to a skewed Gaussian distribution for the average residuals but significantly deviates from this distribution at the extremes. The threshold should consider this behavior. (For interpretation of the references to color in this figure legend, the reader is referred to the web version of this article.)
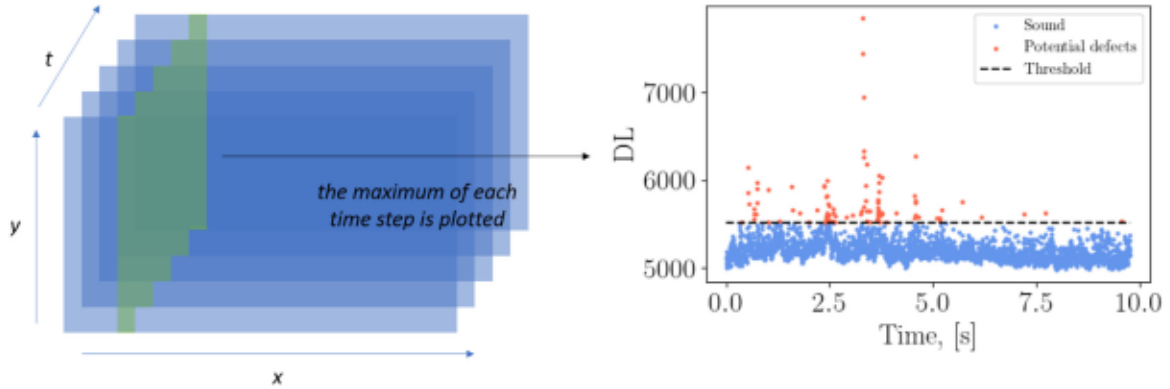

Fig. 9. Graph illustrating the temporal maxima plot for a specific y-spatial column (at a given x position). The threshold is adjusted using the average deviation.

of the parameter β, providing *a priori* information about the distribution of parameter probabilities. In our specific case, a uniform probability density is assumed over the parameter domain $\beta = [0, 1]$ because of the lack of any *a priori* information about the expected fiber content. The last term, $\pi(T_{obs}|\beta)$, is the likelihood function, providing the probability of the temperature field given β. In the case of an additive white Gaussian noise with known variance γ, the temperature field observed can be expressed as Eq. (12) with Y, B and E the random variables associated respectively, with the temperature field, fiber content β and noise ; and f the function describing the model.

$$Y = f(B) + E \tag{12}$$

Hence, the random variable Y shares the same distribution as the noise, given a fixed β [29]. Consequently, the likelihood function can be explicitly formulated, as illustrated in Eq. (13).

$$\pi(T_{obs}|\beta) \propto \exp\left(-\frac{1}{\gamma^2}\|T_{obs} - T_\beta\|_2^2\right) \tag{13}$$

In the end, the estimator of the fiber content β is chosen as the maximum *a posteriori*.

Ultimately, the overarching approach to characterization unfolds as follows: in the initial phase, the baseline fiber content of the composite is determined using the average thermogram of the tape over time. Following the initial estimation, further refinement is carried out, focusing exclusively on estimating the fiber content for the pixels located in regions of the tape where defects have been identified.

4. Experimental results

The whole methodology presented in the previous section is deployed on an experimental case. It consists of a rolling tape moving at a velocity of 15 m/min for a duration of 10 min. It corresponds to approximately 150 meters of material to be characterized and results in the generation of 20 GB of data with the camera parameters described in Section 1.1.

4.1. Defect detection and tracking

After calculating the thresholds defined in Section 3.1 and the velocity described in Section 3.2, frames containing defects were identified and each detected defect was labeled and tracked as shown in Fig. 14.
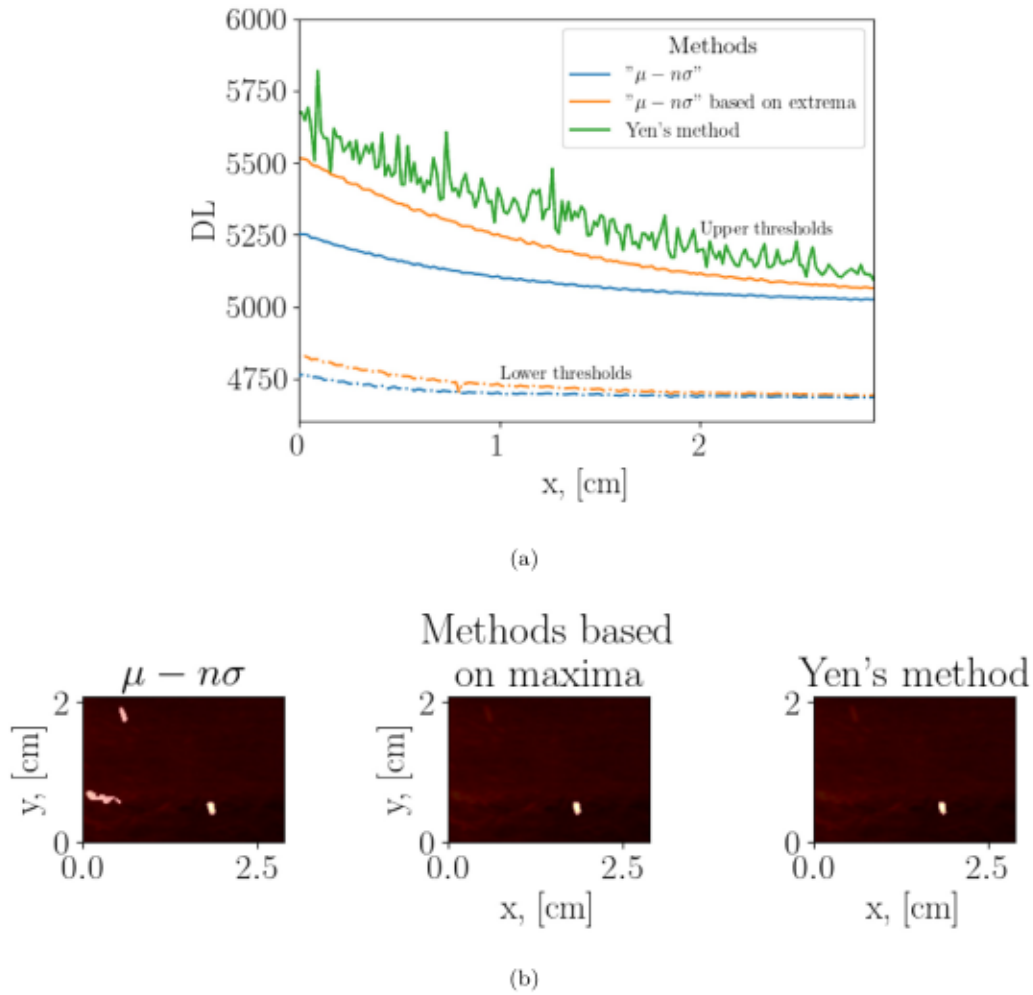
(a)

(b)

Fig. 10. (a) Lower and upper thresholds plotted for the three different methods, with $n = 2$. As observed, the "$\mu - n\sigma$" method is less restrictive than the others on the upper thresholds. The threshold from Yen's method is the most restrictive but is noisy and may not be reliable in the presence of disturbances. For the lower thresholds, the two different methods are similar. (b) Labeling of defects with the different thresholds, with $n = 2$. The threshold from the "$\mu - n\sigma$" method is more tolerant.

(a)

(b)
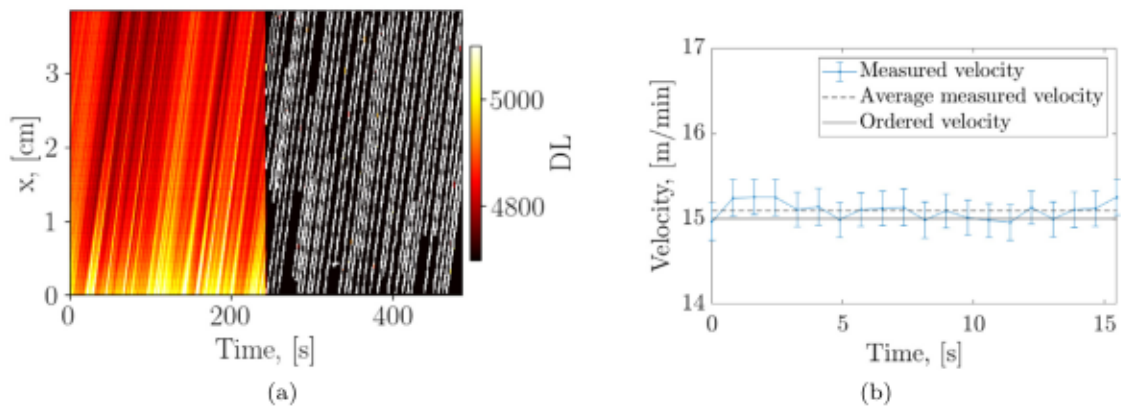
Fig. 11. (a) Left: The temperature distribution is depicted for each parallel line. Right: The application of a Canny filter on the constructed temperature field of the line. (b) Real-time velocity measurement for four distinct sets.

This figure highlights the intensity diminution on the defect area relative to its position in the camera's field of view, and so on the distance to the lamp. Once the defects are detected, the characterization method is applied to the corresponding recorded frames. The characterization is finally performed only on a few portions of the tape, reducing the data volume from 20 GB to less than 0.5 GB, allowing a real time data exploitation.

4.2. Average fiber content measurement

The average fiber content is then measured. To verify the characterization method's robustness and repeatability over the experimental time, average portions of the tape were analyzed. A moving average is applied to each line over 600 time steps, repeated 300 times on a 2 min interval. The Fig. 15(a) displays one of these average curves
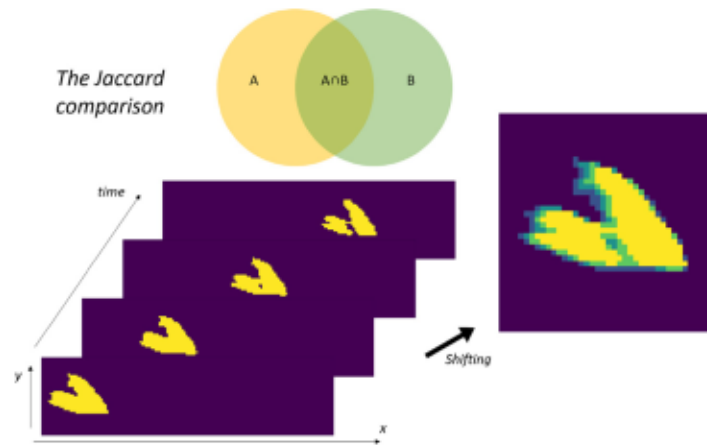
Fig. 12. Calculation framework for Jaccard index [27]. Following the defect labeling phase in an image, images are displaced based on the measured velocity to identify corresponding defects in previous images. The Jaccard index serves as the recognition metric.
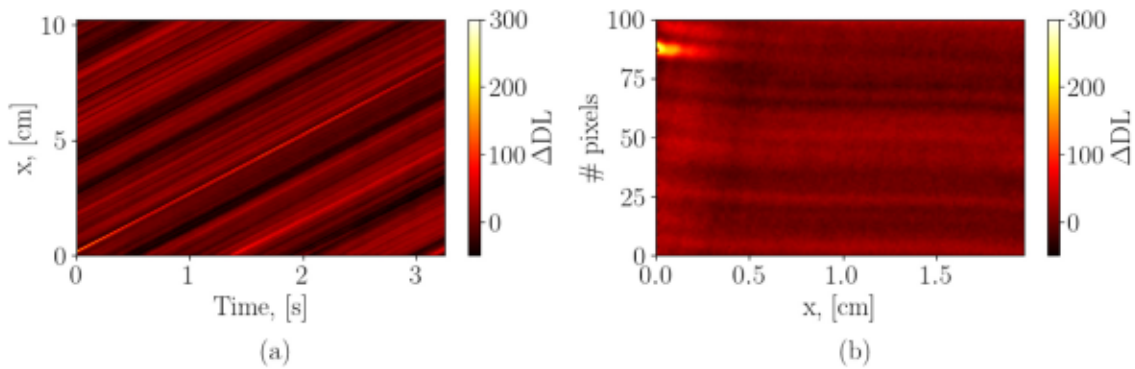

Fig. 13. (a) A temperature distribution is depicted for one line. (b) Reconstructed pseudo-matrix of this line. Each # number of pixels corresponds to each point of the tape on the line. A correction must be carried out to rectify the distortion at the edges.
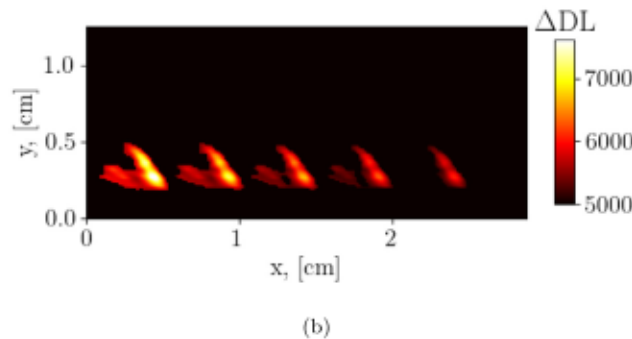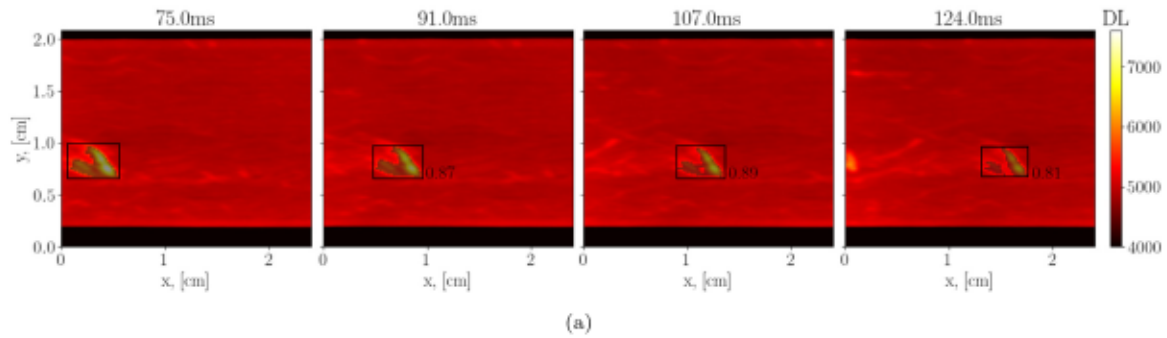

Fig. 14. (a) Monitoring a defect at various positions across the camera's field of view. The numbers adjacent to the boxes represent the Jaccard metrics between consecutive labels. (b) Successive frames of the detected defect. We observe the cooling.
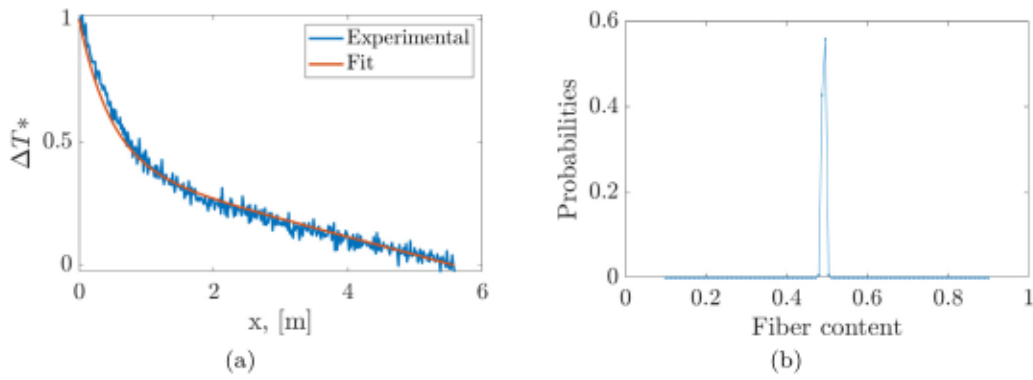
Fig. 15. (a) Average normalized temperature profile: experimental and fit plots. (b) Corresponding obtained normalized *a posteriori* distribution.
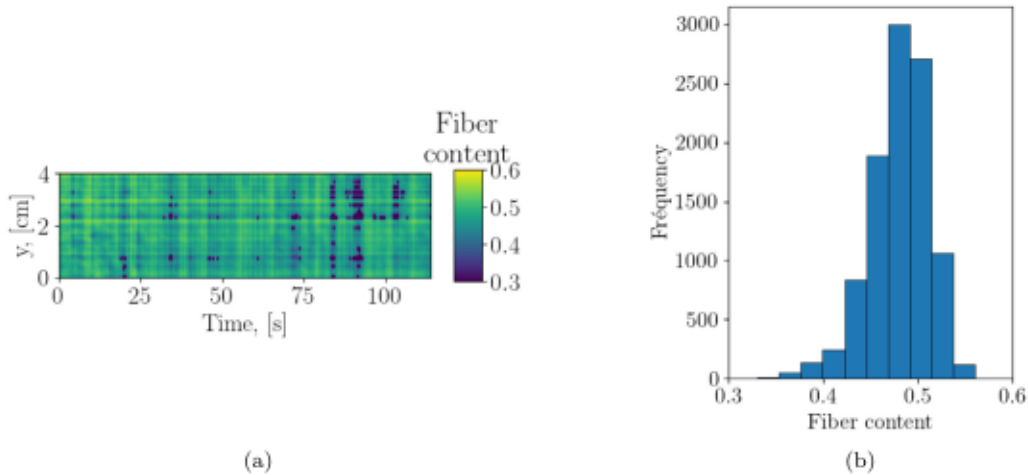

Fig. 16. (a) Estimation of the fiber content on the lines at different times. (b) Distribution of the estimated fiber contents. The average is closed to the predicted value of 0.5.

and its corresponding fit determined using the maximum *a posteriori* estimation (Fig. 15(b)).

A residuals analysis was conducted, revealing that the variance of the residuals is of a similar magnitude to that of the noise ($\gamma_{residuals}$ = 5e-4 and γ_{noise} =3e-4). The results obtained for the entire tape segment are presented in Fig. 16. This finding confirms that the method is capable of accurately estimating the average fiber content of the composite material, providing a reliable baseline for comparison with other measurements. In contrast, the study conducted by K. Miyachi et al. [30] on the measurement of CFRP diffusivity reveals a similar level of variability.

4.3. Defect characterization

For the study of defect characterization, as many data are analyzed, we decided to focus on one specific defect. Once a defect is identified, the characterization process is applied as described, with the Bayesian estimation method. This is performed for each line in the region where the defect occurs. However, in addition to the average fiber content estimation, an essential step of reconstruction of the static thermograms becomes necessary. Some obtained thermograms, taken from Fig. 13, are plotted in Fig. 17. This process enables us to acquire the fiber content for the region surrounding and encompassing the defect, as demonstrated in Fig. 18. As expected, the predominant area has a normal fiber content level, containing no flaws. In the high-intensity areas, the fiber content highly changed. Therefore, defects are characterized by high fiber content. Here, it aligns closely with the findings of K. Miyachi et al. [30], indicating low diffusivity and, consequently, regions of both high and low temperatures where the composite is

inadequately impregnated. It can also be clarified by the findings in the work of V.L. Louët et al. [31], indicating that the absorptivity of the heating is greater in areas with high fiber density on the surface.

A complete portion around the defect is presented in Fig. 19. The whole algorithm runs in less than 2 min on a computer with Intel Core i7 and 32 GB of RAM, which is approximately 10 times faster than the control time.

Conclusion and perspectives

This article proposes a fast algorithm for the detection and characterization of defects on a composite tape. This is achieved through the application of a stochastic method and the separation of the data between flawless and defective portions. The methodology was developed with the objective of real-time implementation to address the necessity for swift control of large quantities of material. This objective is achieved through real-time defect detection and tracking using the "tracking-by-detection" approach. The quantitative algorithm operates concurrently, with a computation time of just a few seconds for each detected anomaly. The results are promising in terms of accurately estimating the average fiber content of the tape and characterizing defects.

Perspectives

The future directions of this research encompass different aspects. Firstly, the identical study with a fixed setup could be employed to obtain an initial depiction of the fiber content distribution and to compare the results from both scans (static and dynamic). Additionally,
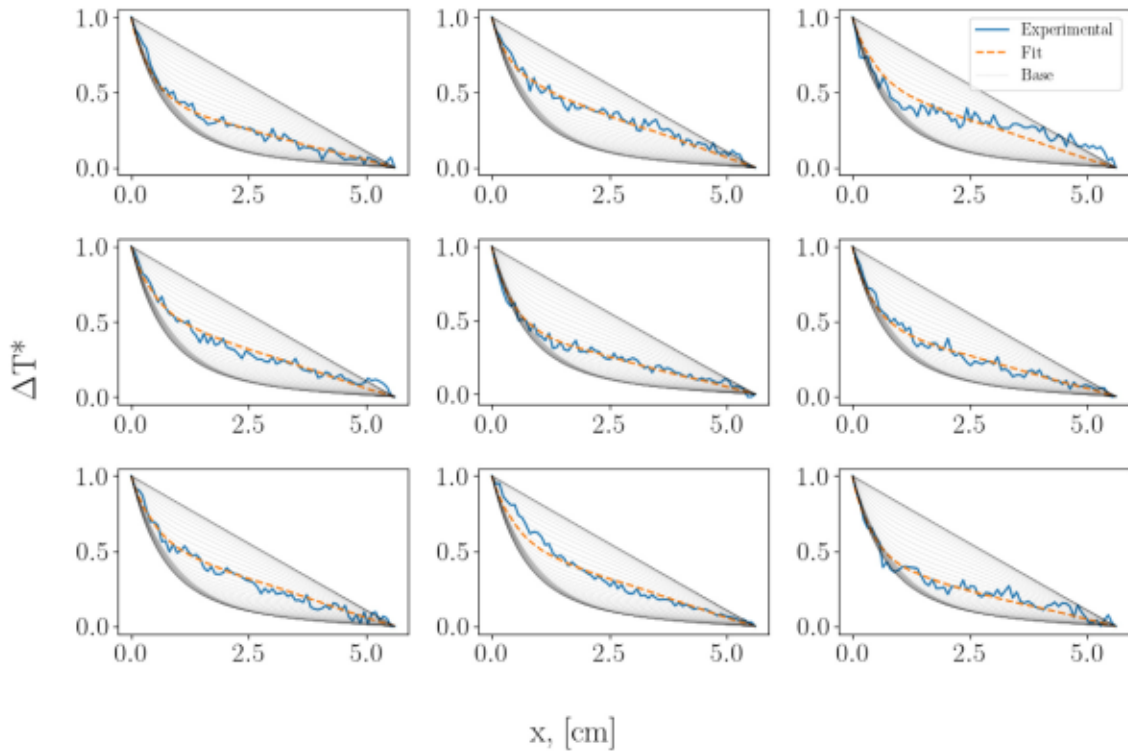
Fig. 17. Random examples of normalized reconstructed static thermograms in blue. In black is plotted the base with which the Bayesian inference is applied and in orange is the corresponding curve of the maximum *a posteriori*. (For interpretation of the references to color in this figure legend, the reader is referred to the web version of this article.)
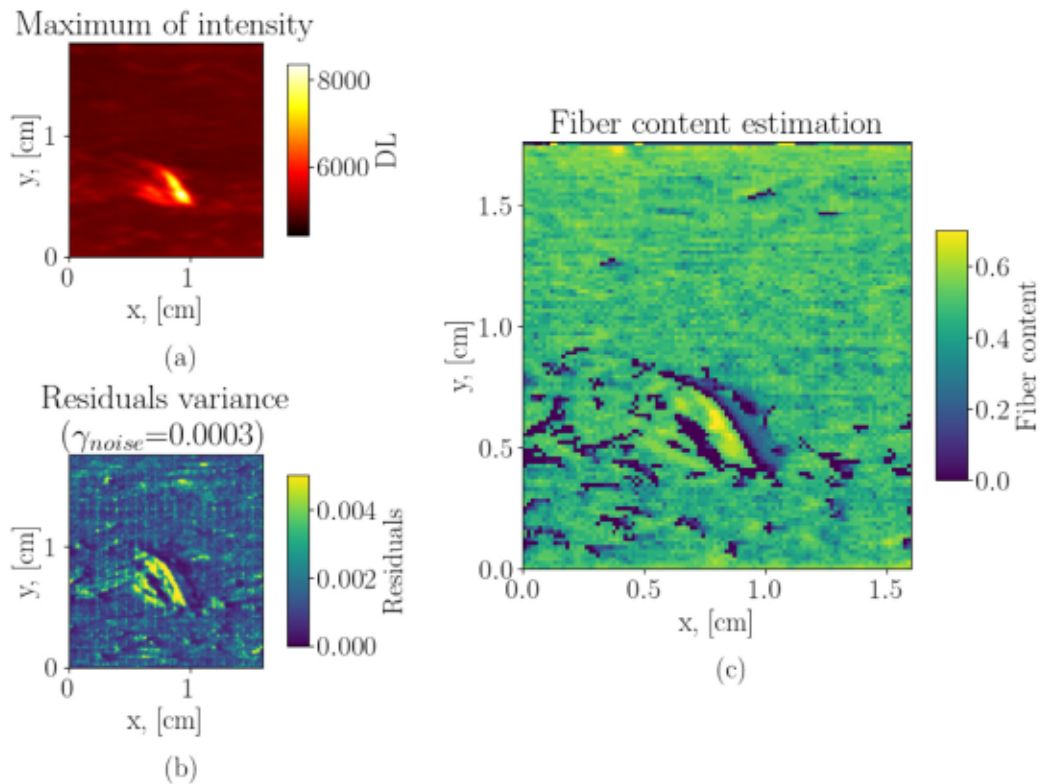

Fig. 18. (a) Maximum intensity reached at each point on the tape. (b) Residuals variance of each pixel. (c) Constructed virtual tape of fiber content properties estimated using the Bayesian method. We identify the area of the defect, with a fiber content estimated lower than 25%.
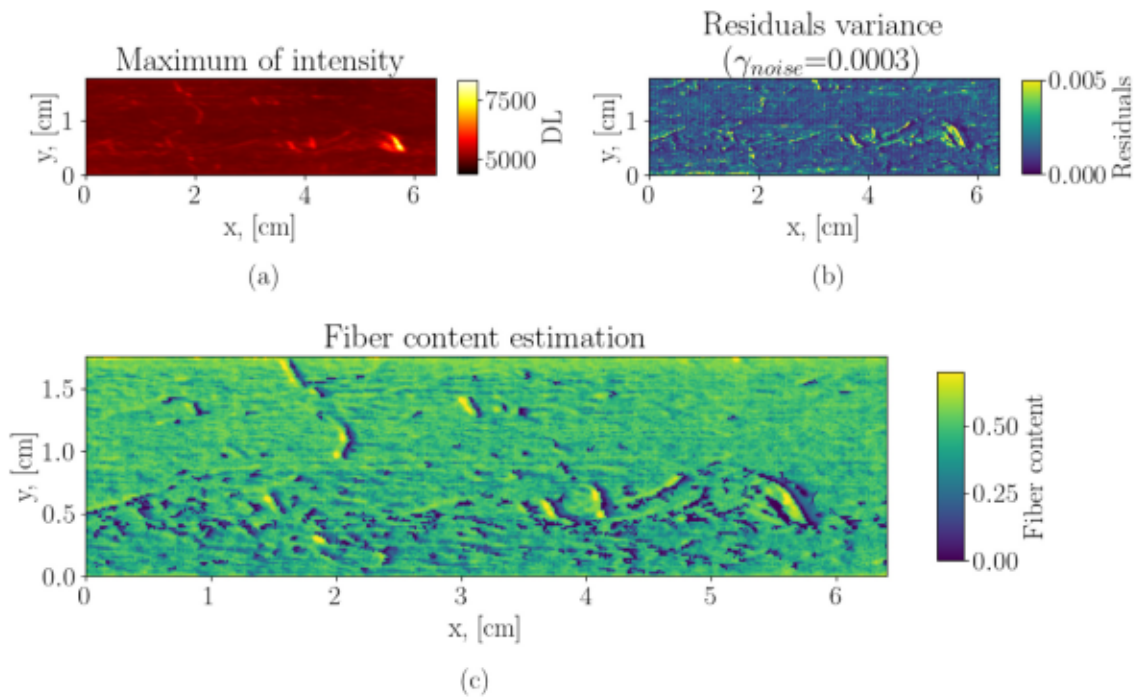
Fig. 19. Complete section around the defect presented in Fig. 18.

method of enhancement of the defects can be analyzed for a better resolution of the defect, as in [32,33].

Therefore, a comparative study with the transmission mode (camera and heating lamp positioned on opposite faces of the composite) could yield additional insights, such as information on thickness variation or the depth of the defects.

Finally, an additional avenue for future research involves investigating the detection of defects deep within laminates or multilayer materials. The sensitivity for these specific defects is weaker due to their depth. Adaptive thresholding techniques must be employed to enhance defect detection capabilities, with for instance a dynamically adjustable threshold level dependent on the depth of the defects to be detected.

CRediT authorship contribution statement

M. Lecorgne: Conceptualization, Formal analysis, Investigation, Methodology, Writing – original draft, Writing – review & editing. **E. Abisset-Chavanne:** Supervision, Validation. **M-M. Groz:** Supervision, Validation. **A. Sommier:** Validation, Visualization. **C. Pradère:** Supervision, Validation.

Declaration of competing interest

The authors declare that they have no known competing financial interests or personal relationships that could have appeared to influence the work reported in this paper.

Data availability

The authors do not have permission to share data.

Acknowledgments

References

[1] Zhang J, Lin G, Vaidya U, Wang H. Past, present and future prospective of global carbon fibre composite developments and applications. Compos B 2023;250:1359–8368, Evolution production de la quantité de tapes de composites.

[2] Fiber tapes market size, share & trend analysis report by form (dry tapes, prepreg tapes), by end use (aerospace & defense, automotive), by region, and segment forecasts, 2020 - 2027). Tech. Rep., Grand View Research; 2020.

[3] Oromiehie E, Prusty BG, Compston P, Rajan G. Automated fibre placement based composite structures: Review on the defects, impacts and inspections techniques. Compos Struct 2019.

[4] Fu Y, Yao X. A review on manufacturing defects and their detection of fiber reinforced resin matrix composites. Compos C 2022;8:100276.

[5] Yadav N, Schledjewski R. Review of in-process defect monitoring for automated tape laying. Composites A 2023;173:107654.

[6] Cui J, Liu W, Zhang Y, Han L, Yin P, Li Y. A visual inspection method for delamination extraction and quantification of carbon fiber reinforced plastic (CFRP). Measurement 2022;196:111252.

[7] Salski B, Gwarek W, Kopyt P, Theodorakeas P, Hatziioannidis I, Koui M, et al. Portable automated radio-frequency scanner for non-destructive testing of carbon-fibre-reinforced polymer composites. J Nondestruct Eval 2016;35:25.

[8] Machado MA, Antin K-N, Rosado LS, Vilaça P, Santos TG. Contactless high-speed eddy current inspection of unidirectional carbon fiber reinforced polymer. Composites B 2019;168:226–35.

[9] Kidangan RT, Krishnamurthy CV, Balasubramaniam K. Identification of the fiber breakage orientation in carbon fiber reinforced polymer composites using induction thermography. NDT E Int 2021;122:102498.

[10] Maldague XPV. Nondestructive evaluation of materials by infrared thermography. London: Springer; 1993.

[11] Zaiß M-L, Jank MH, Netzelmann U, Waschkies T, Rabe U, Herrmann HG, et al. Use of thermography and ultrasound for the quality control of SMC lightweight material reinforced by carbon fiber tapes. Procedia CIRP 2017;62:33–8, Montre l'intérêt d'utiliser la thermographie pour la détection de défauts de quantité de fibres.

[12] Ibarra-Castanedo C, Servais P, Ziadi A, Klein M, Maldague X. RITA - Robotized inspection by thermography and advanced processing for the inspection of aeronautical components. QIRT Council; 2014.

[13] Khodayar F, Lopez F, Ibarra-Castanedo C, Maldague X. Optimization of the inspection of large composite materials using robotized line scan thermography. J Nondestruct Eval 2017;36.

[14] Oswald-Tranta B, Sorger M. Scanning pulse phase thermography with line heating. Quant InfraRed Thermogr J 2012;9:103–22.

[15] Zhang H, Verberne P, Meguid SA, Ibarra-Castanedo C, Maldague XPV. Autonomous high resolution inspection of kiss-bonds skins of carbon nanotube reinforced nanocomposites using novel dynamic line-scan thermography approach. Compos Sci Technol 2020;192:108111.

[16] Moran J, Rajic N. Remote line scan thermography for the rapid inspection of composite impact damage. Compos Struct 2018.

[17] Verspeek S, Gladines J, Ribbens B, Maldague X, Steenackers G. Dynamic line scan thermography optimisation using response surfaces implemented on PVC flat bottom hole plates. Appl Sci (Switzerland) 2021;11:1–15.

[18] André J-C. Industrie 4.0 : paradoxes et conflits. ISTE Group; 2019.

[19] Pabst W, Gregorová E. Effective elastic properties of alumina-zirconia composite ceramics - Part 2. Micromechanical modeling. 2004, Ceramics - Silikaty.

[20] Balageas DL. Defense and illustration of time-resolved pulsed thermography for nde (quantitative InfraRed thermography journal (2012) 9:1 (3-32)). Quant InfraRed Thermogr J 2012;9:231.

[21] Maillet D, André S, Batsale J-C, Degiovanni A, Moyne C. Thermal quadrupoles,solving the heat equation through integral transforms. John Wiley and sons; 2000.

[22] Smalakys L, Švažas E, Grigutis R, Melninkaitis A. Application of image processing and machine learning for classification of laser-induced damage morphology. In: Carr CW, Exarhos GJ, Gruzdev VE, Ristau D, Soileau M, editors. In: Laser-induced damage in optical materials 2018: 50th anniversary conference, vol. 10805, SPIE, International Society for Optics and Photonics; 2018, p. 108052B.

[23] Yen J-C, Chang F-J, Chang S. Correspondence a new criterion for automatic multilevel thresholding. IEEE Trans Image Process 1995;4.

[24] Deng B. Line scanning thermography reconstruction algorithm for defects inspection with novel velocity estimation and image registration. IEEE Sensors J 2021.

[25] Canny JF. Finding edges and lines in images. 1983.

[26] Bochinski E, Eiselein V, Sikora T. High-speed tracking-by-detection without using image information. In: 2017 14th IEEE international conference on advanced video and signal based surveillance. AVSS, 2017, p. 1–6.

[27] Jaccard P. Lois de distribution florale dans la zone alpine. Bull Soc vaudoise Sci Naturelles 1902;38:69–130.

[28] Bayes T, Price n. LII. An essay towards solving a problem in the doctrine of chances. By the late Rev. Mr. Bayes, F. R. S. communicated by Mr. Price, in a letter to John Canton, A. M. F. R. S. Philos Trans R Soc Lond 1763;53:370–418.

[29] Kaipio J, Somersalo E. Statistical and computational inverse problems. Applied mathematical sciences, New York: Springer; 2006.

[30] Miyachi K, Muranaka Y, Nonaka S, Ueno A, Nagano H. Measurement of thermal diffusivity and evaluation of fiber condition of discontinuous fiber CFRP. Infrared Phys Technol 2021;115.

[31] Louët VL, Corre SL, Boyard N, Delaunay D, Tardif X. Experimental characterization of the thermal behavior of carbon/PEEK tapes in the laser-assisted AFP process, vol. 2113, American Institute of Physics Inc.; 2019.

[32] Liu H, Du W, Nezhad HY, Starr A, Zhao Y. A dissection and enhancement technique for combined damage characterisation in composite laminates using laser-line scanning thermography. 2021, http://dx.doi.org/10.1016/j.compstruct.2021.114168.

[33] He Z, Wang H, Li Y, Zhang Z, Zhang Y, Bi H, et al. A deconvolutional reconstruction method based on Lucy-Richardson algorithm for joint scanning laser thermography. IEEE Trans Instrum Meas 2021;70.